Article

Controlled Growth of Porous InBr₃: PbBr₂ Film for Preparation of CsPbBr₃ in Carbon-Based Planar Perovskite Solar Cells

Kailin Chi [1,*], Hansi Xu [1], Bingtao Feng [2], Xianwei Meng [2], Daoyu Yu [1] and Qian Li [3,*]

[1] School of Science, Northeast Electric Power University, Jilin 132012, China; 20182815@neepu.edu.cn (H.X.); 2018309050138@neepu.edu.cn (D.Y.)

[2] State Key Laboratory of Superhard Materials, College of Physics, Jilin University, Changchun 130012, China; fengbt20@mails.jlu.edu.cn (B.F.); xwmeng17@mails.jlu.edu.cn (X.M.)

[3] Beijing Key Lab of Cryo-Biomedical Engineering and Key Lab of Cryogenics, Technical Institute of Physics and Chemistry, Chinese Academy of Sciences, Beijing 100190, China

* Correspondence: kailinchi@neepu.edu.cn (K.C.); liqian@mail.ipc.ac.cn (Q.L.); Tel./Fax: +86-0432-64806674 (K.C.); +86-010-82543763 (Q.L.)

Abstract: Due to the low solubility of CsBr in organic solvents, the CsPbBr₃ film prepared by the multi-step method has holes and insufficient thickness, and the light absorption capacity and current density of the perovskite film hinder the further improvement in the power conversion efficiency (PCE) of CsPbBr₃ solar cells. In this study, we introduced InBr₃ into the PbBr₂ precursor solution and adjusted the concentration of PbBr₂, successfully prepared PbBr₂ with a porous structure on the compact TiO₂ (c-TiO₂) substrate to ensure that it fully reacted with CsBr, and obtained the planar carbon-based CsPbBr₃ solar cells with high-quality perovskite film. The results reveal that the porous PbBr₂ structure and the increasing PbBr₂ concentration are beneficial to increase the thickness of the CsPbBr₃ films, optimize the surface morphology, and significantly enhance the light absorption capacity. Finally, the PCE of the CsPbBr₃ solar cells obtained after conditions optimization was 5.76%.

Keywords: CsPbBr₃; planar perovskite solar cells; InBr₃; porous PbBr₂ film

1. Introduction

From the perspective of the preparation process, a very unique advantage of perovskite solar cells (PSCs) is that they have better processability [1–4]. Whether an organic-inorganic hybrid or all-inorganic perovskite solar cell, the film quality of the perovskite active layer (including morphology, grain shape, grain size, number of grain boundaries, whether there are pinholes, etc.) determines the PCE and durability of PSCs [5–9]. Generally, the prepared perovskite film should have a high-density microstructure, large grain size, low grain boundary density, and no pinholes or other voids in the film, to improve electron/hole mobility, achieve reduction in radiation recombination, and other purposes [1,10–12]. Both the preparation method of the perovskite film and the device structure (planar or mesoporous structure) can exert a significant impact on the quality and photoelectric performance of the perovskite film. In the process of preparing perovskite films by the two-step method, mesoporous substrates are often used to promote the PCE of PSCs. This is because the mesoporous layer formed by oxide nanoparticles has a higher specific surface area, and a large number of pores promote the improvement in the effective diffusivity of the lead halide precursor solution [13], so denser lead halide nanosized grains can be generated faster in the mesoporous layer, and the conversion process of lead halide to perovskite can be accelerated [1,14]. However, during this conversion process, due to some unconverted lead halide residues in the mesoporous layer and the possible formation of random crystals in the perovskite film [14,15], the efficiency of PSCs may be greatly affected. A method for fully converting the lead halide is a critical prerequisite for controlling the growth of perovskite films, or ensuring the perfect formation of crystals and enhancing the efficiency of PSCs [16–18].

Introducing a porous lead halide film into a planar structure is an effective method to replace the mesoporous structure in the two-step method [1]. The porous structure in the lead halide film can enlarge the contact area between the lead halide and other precursor solutions and increase the reaction rate, and it can reduce space-expansion-induced defects and residual stress during the expansion of the film [5]. Liu et al. [19] spin-coated a solution of PbI_2 in DMF onto a substrate, then prepared a PbI_2 film with a porous structure by adjusting the standing time. Ostwald ripening of the PbI_2 crystallites can result in larger crystals and increase the void space between grains. The increase in porosity in the PbI_2 film effectively promotes the transformation process of perovskite and reduces the residual amount of PbI_2. The resulting $CH_3NH_3PbI_3$ PSCs with inverted planar heterojunction have an efficiency of 15.7%, and there is almost no hysteresis. Dong et al. [20] confirmed that the porosity in PbI_2 can affect the phase composition and film morphology of $CsPbI_2Br$. Compared with other anti-solvents, the PbI_2 (DMSO) film treated with green ethanol has higher porosity and randomly distributed crystals, which provide more diffusion paths and contact areas for the CsBr precursor, and create an essential prerequisite for ultimately obtaining $CsPbI_2Br$ film with high purity, high thickness, large grains, and full coverage. Although the $CsPbBr_3$ film prepared by the multi-step method exhibits excellent moisture and thermal stability [21–24], it is also prone to problems such as low film coverage, thin film thickness, and the presence of impurity phases (such as $CsPb_2Br_5$) [5,25,26]. As mentioned above, a porous $PbBr_2$ film with higher porosity can provide more diffusion paths for the CsBr precursor and increase the contact area between the two, which ultimately provides a favorable condition for the formation of $CsPbBr_3$ with high purity phase and high coverage [27–29]. Zhao et al. [21] prepared porous $PbBr_2$ films on SnO_2 substrates by precisely controlling the crystallization temperature. The porous structure of $PbBr_2$ not only allows the effective diffusion of CsBr solution to gain high-purity $CsPbBr_3$, but also offers enough space for the growth of $CsPbBr_3$ grains under stress-free conditions, resulting in high-quality $CsPbBr_3$ film with larger grain size and lower grain boundary density. In our previous work, we prepared porous $PbBr_2$ films on mesoporous TiO_2 (m-TiO_2) by introducing $InBr_3$ into the $PbBr_2$ precursor solution, and achieved In^{3+} or In cluster doping with $CsPbBr_3$, thereby improving the growth quality of $CsPbBr_3$ films and enhancing the efficiency of $CsPbBr_3$ solar cells with mesoporous structure [30].

At present, it is a highly attractive choice to use carbon electrodes, which are low cost and highly stable, to construct $CsPbBr_3$ PSCs without hole transport layer (HTL). Carbon, which matches the work function of perovskite, can effectively transport holes, and avoid the instability of traditional organic HTL (such as Spiro-MeOTAD) and the low conductivity of metal oxide HTL. At the same time, compared with Au electrodes, the carbon electrode is lower cost, and does not diffuse into the perovskite and cause the device performance to deteriorate as does the Ag electrode [31–33]. On the basis of our previous research results, in this work, we introduced $InBr_3$ into a $PbBr_2$ precursor solution and adjusted the concentration of $PbBr_2$ to prepare a high-quality $CsPbBr_3$ film with high thickness, high density, and no holes on c-TiO_2, in order to further simplify the structure of the $CsPbBr_3$ PSCs and optimize the growth quality of the $CsPbBr_3$ film. When the concentration of $InBr_3$ is 0.21 M and $PbBr_2$ concentration is 1.3 M, the prepared carbon-based $CsPbBr_3$ solar cells with a planar structure show the best 5.76% PCE with a short circuit current density (J_{SC}) of 6.52 mA/cm^2, an open circuit voltage (V_{OC}) of 1.29 V, and a fill factor (FF) of 0.68.

2. Materials and Methods

2.1. Materials

The fluorine-doped tin oxide coated glass (FTO, 6 $\Omega/\square$) was purchased from Opvtech New Energy Co., Ltd. (Yingkou, China). Titanium (IV) isopropoxide (99.9%), N,N-dimethylformamide (DMF, chromatographic grade, $\geq$99.9%), methanol (chromatographic grade, $\geq$99.9%), ethanol (chromatographic grade, $\geq$99.8%), and isopropanol ($\geq$99.5%) were purchased from Aladdin (Shanghai, China). $PbBr_2$ (99.99%) and CsBr

(99.9%) were purchased from Xi'an Polymer Light Technology Corp (Xi'an, China). $InBr_3$ (99.9%) was purchased from Macklin Biochemical Co., Ltd. (Shanghai, China). The commercial carbon paste was purchased from Shanghai MaterWin New Materials Co., Ltd. (Shanghai, China).

2.2. Device Fabrication

All the following processes were carried out in an air atmosphere. The c-TiO_2 was spin-coated on pretreated FTO substrates using 0.2 M titanium isopropoxide in ethanol at 5000 rpm for 30 s and dried for 10 min at 120 °C, then the substrates were annealed at 500 °C for 1 h. Perovskite films were synthesized by a multistep solution-processing method. We added 0.21 mmol of $InBr_3$ to 1 mL DMF solution of 1.0, 1.1, 1.2, 1.3, or 1.4 M $PbBr_2$, which was stirred under 90 °C. Afterward, the mixed solution was spin-coated on the FTO/c-TiO_2 substrate at 2000 rpm for 30 s and heated to 90 °C for 30 min to obtain $InBr_3$:$PbBr_2$ films with a porous structure. Then, the methanol solution of CsBr (0.07 M) was spin-coated on $InBr_3$:$PbBr_2$ film at 5000 rpm for 30 s and continuingly heated at 250 °C for 5 min. This step was performed 6 times. After the prepared sample was soaked in isopropanol for 30 min and annealed at 250 °C for 15 min, the blade coating method was applied to coat carbon paste onto the perovskite films and heated at 100 °C for 10 min to form the carbon back electrode with the effective area of 0.09 cm^{-2}.

2.3. Characterization

The X-ray diffraction (XRD) patterns of the synthesized sample were investigated using an X-ray diffractometer (Cu Kα radiation, λ = 1.5418 Å, Rigaku D/max2500, Tokyo, Japan). The morphologies of the synthesized films were recorded by a scanning electron microscope (SEM, FEI MAGELLAN 400, FEI, Hillsboro, OR, USA), and the system was connected to an energy-dispersive X-ray spectroscopy (EDS). X-ray photoelectron spectroscopy (XPS) was performed by an X-ray photoelectron spectrometer system (K-Alpha, Thermo Fisher Scientific, Waltham, MA, USA) equipped with a monochromatic Al Kα X-ray source (1486.6 eV) operating at 100 W. The steady-state photoluminescence (PL) and the time-resolved photoluminescence (TRPL) decay spectrums of perovskite films were collected on a photoluminescence spectrometer (FLS980, Edinburgh Instruments, Livingston, UK) with a 473 nm excitation source. The absorption spectrum was measured by a UV–Vis spectrometer (UV-3600, Shimadzu, TKY, Japan) in the range of 200 to 800 nm. The current–voltage (*J*–*V*) characteristics were measured by a solar cells test system (XP3000, Sanyou, China) equipped with a Keithley 2400 source meter. The external quantum efficiency (EQE) was tested by an EQE measured system (QTest Station 1000A, CROWNTECH, INC., Macungie, PA, USA) under DC mode.

3. Results and Discussion

Figure 1 displays the top-view SEM images prepared without and with introducing 0.21 M $InBr_3$ in $PbBr_2$ precursors of different solubility. When the $PbBr_2$ precursor concentration was 1.0 M without introducing $InBr_3$, the $PbBr_2$ film produced was uniform, dense, crack-free, and had a smooth surface, and there were pores of different sizes in the film (Figure 1a). In contrast, after the introduction of $InBr_3$ into the 1.0 M $PbBr_2$ precursor solution, as shown in Figure 1b, the $InBr_3$:$CsPbBr_3$ film had a porous structure, the crystal grains were mostly block structures with obvious size differences, and there were relatively small gaps between the crystal grains. This indicates that $InBr_3$ can transform the $PbBr_2$ grown on the c-TiO_2 substrate from a dense film to a relatively low-density porous film. Compared with the porous $PbBr_2$ film formed on m-TiO_2, the morphology of the $PbBr_2$ film prepared on c-TiO_2 changed significantly regardless of the introduction of $InBr_3$, which reveals that both the TiO_2 substrate and $InBr_3$ can directly affect the morphology of the $PbBr_2$ film and determine the quality of the subsequent $CsPbBr_3$ film growth. With the further increase in the $PbBr_2$ concentration (1.1~1.4 M), although the films prepared under various conditions were still porous films, the morphology and porosity of the films did

not illustrate obvious differences. The columnar and cubic crystal grains grouped into clusters, with gaps between the clusters, which provide space for the subsequent growth and free expansion of $CsPbBr_3$ crystals [13,34]. Based on the cross-sectional SEM images of the corresponding $PbBr_2$ films (Figure S1, Supplementary Materials), it can be concluded that the thickness of the film (330, 400, 450, 500, and 550 nm), the grain size, and the gap between the crystal grains (clusters) all exhibit an increasing trend with the increase in the $PbBr_2$ concentration, which provides the pivotal condition to enhance the diffusion rate of the CsBr precursor and increase the contact area and reaction efficiency between CsBr and $PbBr_2$, and subsequently guarantee the production of high-quality $CsPbBr_3$ films with high thickness, high purity, high density, and large crystal grains.
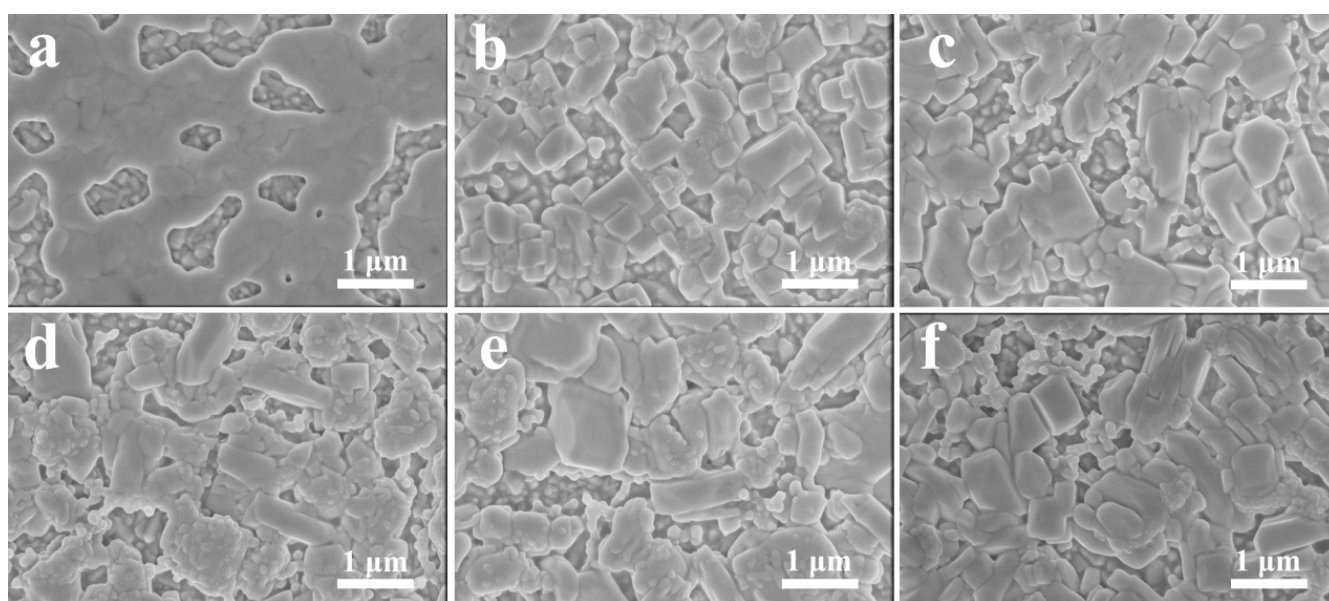

Figure 1. Top-view SEM images of $PbBr_2$ films synthesized with different $PbBr_2$ concentration: (**a**) 1.0 M w/o $InBr_3$; (**b**) 1.0 M w/ $InBr_3$; (**c**) 1.1 M w/ $InBr_3$; (**d**) 1.2 M w/ $InBr_3$; (**e**) 1.3 M w/ $InBr_3$; (**f**) 1.4 M w/ $InBr_3$.

To validate the influence of porous lead bromide films made by introducing $InBr_3$ on the morphologies of the $CsPbBr_3$ films, the top-view and cross-sectional SEM images illustrated in Figure 2 were examined. When the $PbBr_2$ precursor concentration was 1.0 M without introducing $InBr_3$, that is, when the $PbBr_2$ film was a flat film, the thickness of the obtained $CsPbBr_3$ film was about 290 nm, the film showed poor uniformity and coverage, and many holes in the film (Figure 2a). With the further increase in $PbBr_2$ concentration (1.1~1.4 M), the thickness of each perovskite film was 310, 330, 350, and 370 nm, respectively (Figure S2, Supplementary Material). When 0.21 M $InBr_3$ was introduced into the $PbBr_2$ precursor solution, with the increase in the $PbBr_2$ concentration (1.0~1.3 M), the $CsPbBr_3$ film showed a satisfying growth relationship with c-TiO_2, and the film thickness significantly increased to approximately 430, 470, 500, and 540 nm, respectively, which reveals that the porous structure of the $PbBr_2$ film is the main factor affecting the increase in the thickness of the $CsPbBr_3$ film. Meanwhile, the coverage of the $CsPbBr_3$ film gradually rose with the increase in the $PbBr_2$ concentration, with the pores in the film gradually decreasing, the average size of the crystal grains increasing, and the density and uniformity of the perovskite film significantly improving. In particular, when the $PbBr_2$ concentration was 1.3 M, the surface of the $CsPbBr_3$ film was smooth and dense with almost no holes. As mentioned above, the porous structure of the $PbBr_2$ film can increase the contact area between the CsBr precursor and $PbBr_2$ and make the two fully react, thereby making the process of converting $PbBr_2$ to $CsPbBr_3$ faster and more complete. With the increase in the $PbBr_2$ concentration, that is, as the gap between the $PbBr_2$ crystal grain clusters gradually enlarges, more uniform perovskite nuclei with a narrower size distribution are

generated in the porous $PbBr_2$ film in a shorter time. Small grains with unfavorable growth orientation transfer their monomers through the solid-state grain boundary to at least a few larger grains with decent growth orientation, until smaller grains disappear to generate large grains with the largest surface and interface area, and finally producing a large-grain $CsPbBr_3$ film that completely covers the substrate and has no holes [1,35]. However, as the concentration of the $PbBr_2$ precursor containing $InBr_3$ was further increased to 1.4 M, the thickness of the formed $CsPbBr_3$ film further increased to about 580 nm, but the surface morphology of the $CsPbBr_3$ film began to deteriorate, and holes appeared in the film again, which can adversely affect the J_{SC} of $CsPbBr_3$ solar cells [36].
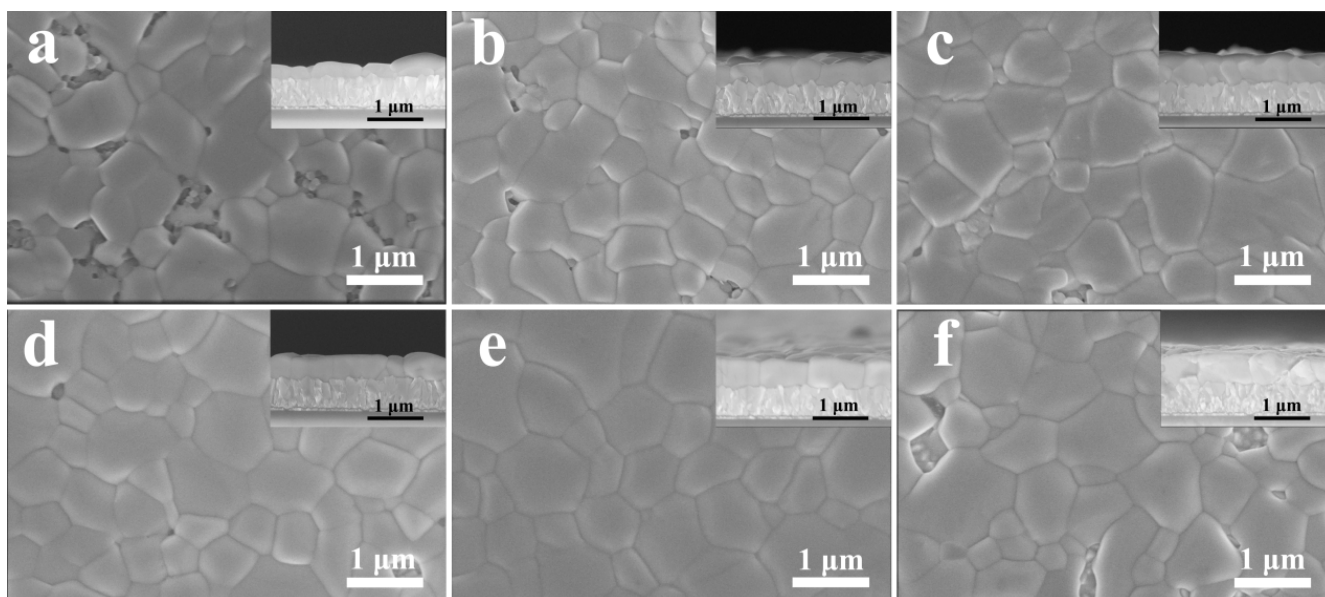

Figure 2. Top-view and cross-sectional (insets) SEM images of $CsPbBr_3$ films synthesized with different $PbBr_2$ concentration: (**a**) 1.0 M w/o $InBr_3$; (**b**) 1.0 M w/ $InBr_3$; (**c**) 1.1 M w/ $InBr_3$; (**d**) 1.2 M w/ $InBr_3$; (**e**) 1.3 M w/ $InBr_3$; (**f**) 1.4 M w/ $InBr_3$.

To investigate the effect of porous $PbBr_2$ film on the phase, structure, and element composition of the perovskite, the XRD and EDS mappings were employed to characterize the $CsPbBr_3$ films. The XRD patterns demonstrated in Figure 3a reveal that all $CsPbBr_3$ films are cubic structures (PDF# 54-0752) [21,37], which reflects that the introduction of $InBr_3$ and the concentration change of the $PbBr_2$ film will not change the phase of $CsPbBr_3$. When the $PbBr_2$ precursor concentration was 1.0 M without introducing $InBr_3$, a strong diffraction peak belonging to the $PbBr_2$-rich $CsPb_2Br_5$ phase appeared at 2θ of 11.7°. In contrast, after introducing $InBr_3$ into the 1.0 M $PbBr_2$ precursor, the diffraction peak belonging to $CsPb_2Br_5$ phase disappeared ($CsPb_2Br_5$ will not be completely consumed), but the diffraction peak belonging to Cs_4PbBr_6 phase appeared at 2θ of 12.7°. This is because after the porous $PbBr_2$ film with low thickness is fully contacted with the CsBr solution and is completely consumed, the excess CsBr and $CsPbBr_3$ continue to react and form a CsBr-rich Cs_4PbBr_6 phase. On the contrary, in the planar structure of $PbBr_2$, the contact area and the reaction efficiency between CsBr and $PbBr_2$ are relatively low, and thus $PbBr_2$ is not fully consumed. After the introduction of $InBr_3$, as the concentration of the $PbBr_2$ precursor gradually increased from 1.1 to 1.4 M, the intensity of the diffraction peaks belonging to the $CsPb_2Br_5$ phase in the XRD patterns of each sample showed an upward trend, and no obvious diffraction peak belonging to Cs_4PbBr_6 phase was observed. The cross-sectional EDS mapping of the $CsPbBr_3$ film shown in Figure 3b proves that Cs, Pb, Br, and In are evenly distributed in the analyzed area, and there is no Pb or In gathering in a certain area.
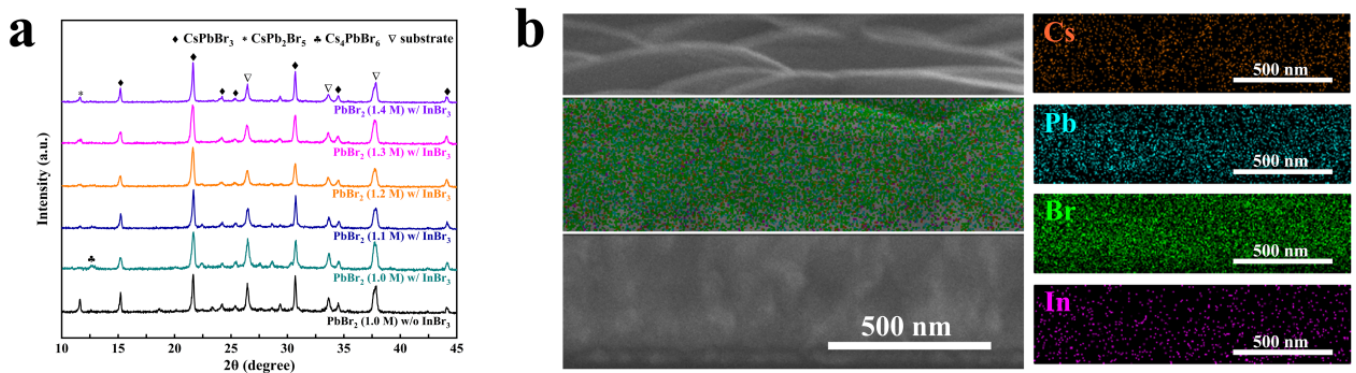
Figure 3. (**a**) XRD patterns of InBr$_3$:CsPbBr$_3$ films synthesized with different PbBr$_2$ concentration; (**b**) elemental distribution mapping images of the InBr$_3$:CsPbBr$_3$ synthesized with the PbBr$_2$ concentration of 1.3 M.

Afterward, we coated the prepared CsPbBr$_3$ films with commercial carbon paste, and dried them to obtain the planar HTL-free PSCs with the structure of FTO/c-TiO$_2$/CsPbBr$_3$/carbon; the cross-sectional SEM image of the device is shown in Figure 4a. In order to further explore the effect of PbBr$_2$ porous film on the device performance, Figure 4b–f illustrates the *J–V* curves under reverse scanning of the PSCs prepared under the conditions of different concentrations of PbBr$_2$ precursor solutions without and with introducing 0.21 M InBr$_3$, and the corresponding parameters are summarized in Table 1. When the PbBr$_2$ concentration was gradually increased from 1.0 to 1.4 M without introducing InBr$_3$ into the precursor solution, the efficiency of each CsPbBr$_3$ cell was at a relatively low level, and there was little difference in the results. It is noteworthy that the efficiency of the CsPbBr$_3$ cell obtained under the condition of a PbBr$_2$ concentration of 1.2 M was the highest, namely 1.79%, while the efficiency of the other cells was between 1.5% and 1.7%. After the introduction of InBr$_3$ into the PbBr$_2$ precursor solution, the efficiency of all PSCs was significantly improved. As the PbBr$_2$ concentration increased from 1.0 to 1.3 M, J$_{SC}$, V$_{OC}$, FF, and PCE all showed a trend of increasing with the increase in PbBr$_2$ concentration. When the PbBr$_2$ concentration was 1.3 M, the champion device with a PCE of 5.76% showed a J$_{SC}$ of 6.52 mA/cm^2, a V$_{OC}$ of 1.29 V, and an FF of 0.68. When the PbBr$_2$ concentration was further increased to 1.4 M, the efficiency of the device decreased to 4.97%, and J$_{SC}$, V$_{OC}$, and FF also illustrated a slight decline, caused by the slight deterioration in the morphology of CsPbBr$_3$. The statistics of photovoltaic parameters collected from 15 devices (Figure S3, Supplementary Materials) and the average photovoltaic parameters with a small standard deviation (Table S1, Supplementary Materials) demonstrate that the InBr$_3$:CsPbBr$_3$ PSCs synthesized with different PbBr$_2$ concentrations obtained in this work have decent reliability and reproducibility. Figure 4g displays the EQE and the corresponding integrated photocurrent densities to verify the validity of the CsPbBr$_3$ devices based on InBr$_3$. The photoresponse edges of these five devices are all around 540 nm. When the PbBr$_2$ concentration is 1.3 M and the maximum EQE value of the champion device is 83%, the EQE values in the light absorption wavelength range of 350–525 nm are significantly enhanced, which proves that the device has better charge injection ability and collection capacity. In addition, the integrated photocurrent density of each device is closer to the corresponding J$_{SC}$, and the mismatch is less than 5%, which signifies the reliability of the *J–V* curves.
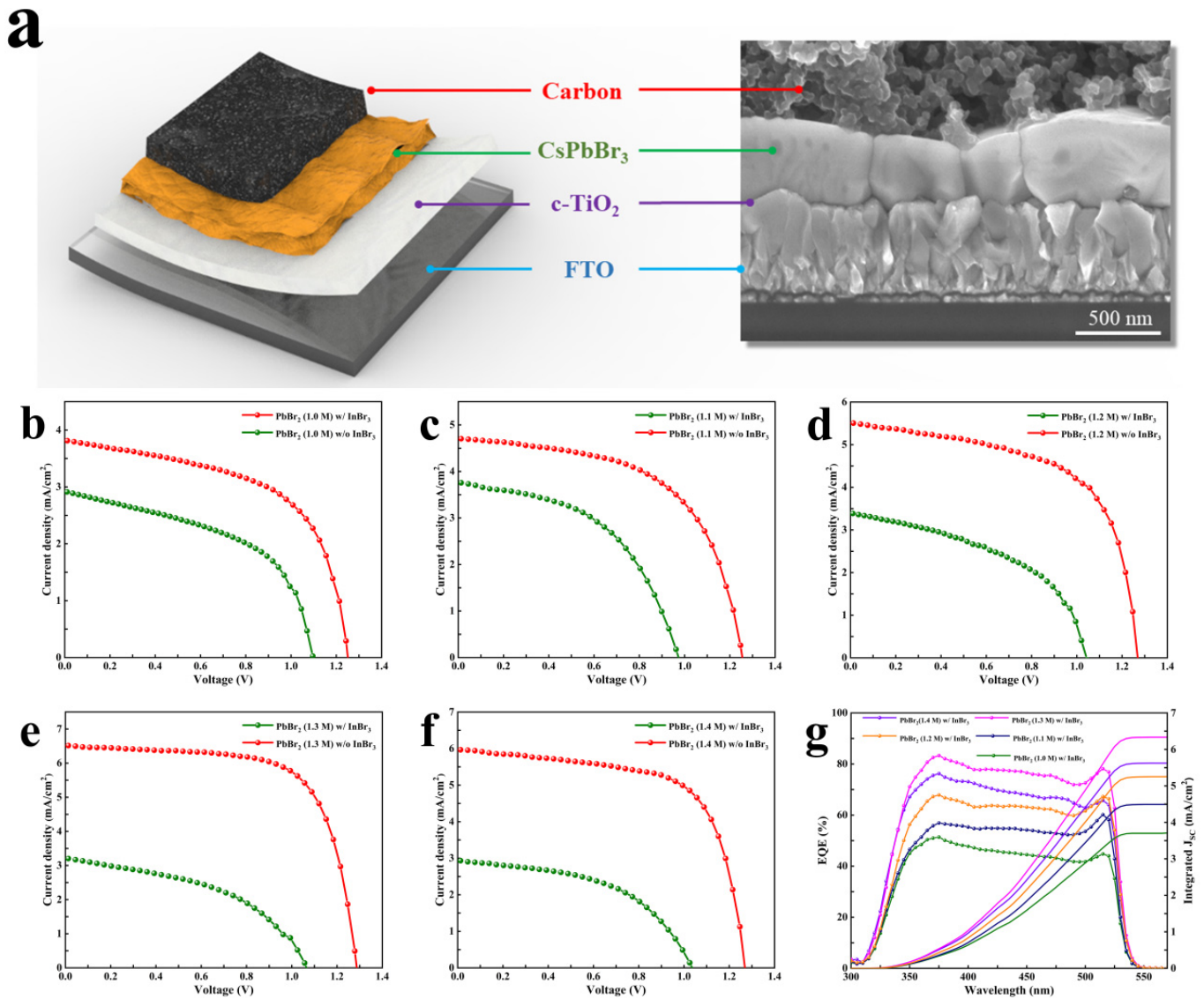
Figure 4. (**a**) Cross-sectional SEM image of the InBr₃:CsPbBr₃ device; (**b–f**) *J–V* characteristics and (**g**) EQE spectra and integrated photocurrent densities for the InBr₃:CsPbBr₃ devices synthesized with different PbBr₂ concentrations.

Table 1. Key *J-V* parameters of the corresponding CsPbBr₃ solar cells.

CsPbBr₃		J_{SC} (mA/cm²)	V_{OC} (V)	FF	PCE (%)
1.0 M	**w/o InBr₃**	2.97	1.09	0.50	1.62
	w/ InBr₃	3.82	1.25	0.57	2.72
1.1 M	**w/o InBr₃**	3.47	0.97	0.49	1.79
	w/ InBr₃	4.70	1.26	0.57	3.38
1.2 M	**w/o InBr₃**	3.40	1.04	0.47	1.66
	w/ InBr₃	5.51	1.27	0.60	4.20
1.3 M	**w/o InBr₃**	3.22	1.07	0.46	1.58
	w/ InBr₃	6.52	1.29	0.68	5.76
1.4 M	**w/o InBr₃**	2.94	1.04	0.50	1.53
	w/ InBr₃	5.97	1.27	0.65	4.97

Furthermore, XPS was utilized to study the influence of InBr₃ on the electronic state of CsPbBr₃ films at a PbBr₂ concentration of 1.3 M. As displayed in Figure 5a, compared

with the pure $CsPbBr_3$, in addition to Cs 3d, Pb 4f, and Br 3d, In 3d was found in the XPS spectra for $InBr_3$: $CsPbBr_3$ film. According to Figure 5b, In $3d_{5/2}$ and In $3d_{3/2}$ peaked at 444.9 eV and 452.3 eV, respectively, and the high-resolution core-level binding energies of Cs 3d, Pb 4f, and Br 3d all shifted toward higher values compared with those in the pure $CsPbBr_3$, which indicates that part of the In(III) in the porous $PbBr_2$ was doped into the perovskite lattice in the process of transforming $CsPbBr_3$, and caused the chemical state of $[PbBr_6]^{4-}$ octahedron to change [38]. The incorporation of In^{3+} or In cluster not only improves the spatial symmetry of the $CsPbBr_3$ lattice structure, but also reduces vacancy defects, which is beneficial to the extraction and transfer process of the charge, and finally significantly optimizes the J_{SC} of the device [30,38–40].
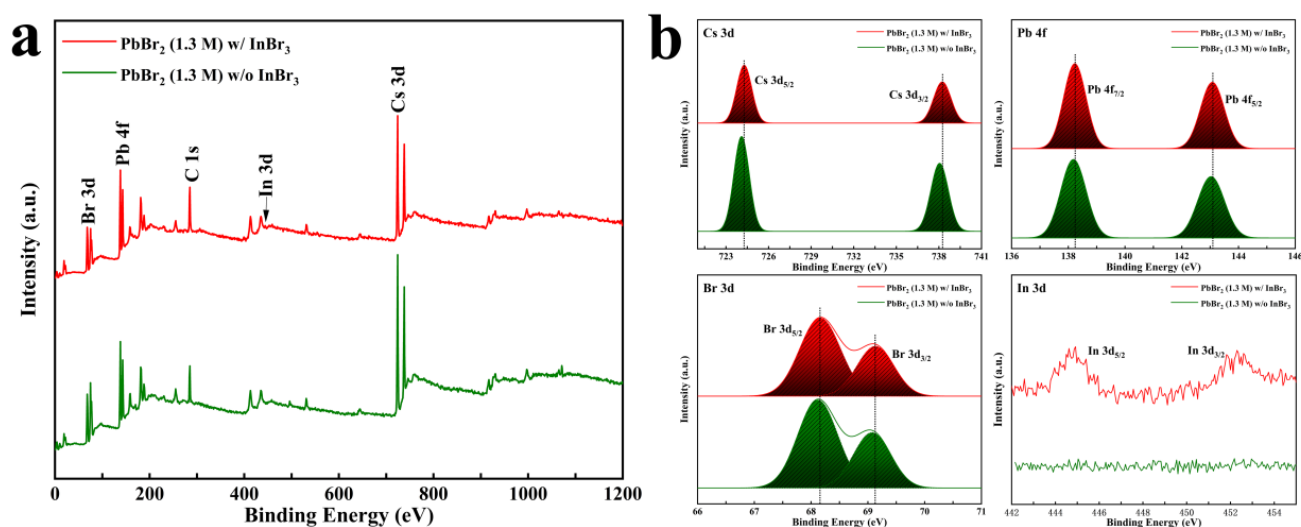

Figure 5. (**a**) XPS spectra and (**b**) Cs 3d, Pb 4f, Br 3d, and In 3d core spectra of the $InBr_3$:$CsPbBr_3$ synthesized with the $PbBr_2$ concentration of 1.3 M.

In the optical property test, the devices with the $FTO/c-TiO_2/CsPbBr_3$ structure were further characterized by a UV–visible spectrophotometer and PL. In Figure 6a, as expected, the absorption edges of all perovskite films are at around 533 nm, which is basically the same as the EQE test result. The light absorption capacity of the films shows a trend of first increasing and then decreasing with increasing $PbBr_2$ concentration, which is consistent with the change law of the perovskite morphology and PCE. In other words, the increase in the thickness of the $CsPbBr_3$ film and the optimization of the surface morphology can enhance the light absorption rate of the perovskite layer and reduce the light loss, which is conducive to generating more electrons to improve J_{SC}. Using Tuac's equation, we can calculate the corresponding band gap (E_g) patterns of the $CsPbBr_3$ film; the curves of α^2 versus the photon energy hν, as shown in Figure 6b; and the E_g of the prepared $CsPbBr_3$ to be about 2.35 eV. Regardless of whether $InBr_3$ was introduced into the $PbBr_2$ precursor, the solubility of $PbBr_2$ did not meaningfully change the E_g of $CsPbBr_3$. Figure S4 (Supplementary Material) illustrates the PL spectra of the PSCs prepared under different concentrations of $PbBr_2$ precursor solutions with introducing 0.21 M $InBr_3$. All the $InBr_3$:$CsPbBr_3$ films presented a typical emission band around 523 nm, which is close to their optical band gap. The PL intensity decreased as the $PbBr_2$ concentration increased from 1.0 to 1.3 M, and then increased as the $PbBr_2$ concentration further increased to 1.4 M. The $InBr_3$:$CsPbBr_3$ film synthesized with the $PbBr_2$ concentration of 1.3 M showed the lowest PL intensity. When the $PbBr_2$ precursor concentration was 1.3 M with/without introducing $InBr_3$, as shown in Figure 6c, the PL peaks for both the $CsPbBr_3$ films were still at about 523 nm, which indicates that the change in the concentration of $PbBr_2$ and the introduction of $InBr_3$ do not change the band position. However, the perovskite prepared after the introduction of $InBr_3$ into the $PbBr_2$ precursor

solution showed more observable strong quenching, which proves that the incorporation of In^{3+} or In cluster and the improvement of perovskite film growth quality are beneficial to faster electron injection and collection, and reduce the recombination of electrons and holes [41,42], which explains why the J$_{SC}$ and V$_{OC}$ of the PSCs were significantly improved after the introduction of InBr$_3$ in Figure 4b–f. Figure 6d illustrates the TRPL decay curves, and the relevant detailed parameters of the corresponding CsPbBr$_3$ films are listed in Table S2. The specific lifetime of the carriers can be determined by a bi-exponential formula $I = A_1 e^{-(\tau - \tau_0)/\tau_1} + A_2 e^{-(\tau - \tau_0)/\tau_2}$ (A$_1$ and A$_2$ are the relative amplitude, respectively; τ_1 and τ_2 are the fast and slow decay time, respectively) [43], and the average lifetimes (τ_{ave}) is calculated by the formula $\tau_{ave} = (A_1 \tau_1^2 + A_2 \tau_2^2)/(A_1 \tau_1 + A_2 \tau_2)$ [44]. Significantly decreased lifetimes of τ_1, τ_2, and τ_{ave} of the InBr$_3$:CsPbBr$_3$ film (1.35, 3.06 and 2.49 ns, respectively) compared with the control CsPbBr$_3$ (2.65, 5.61, and 3.95 ns, respectively) were observed, representing lower trap states in the InBr$_3$:CsPbBr$_3$ film and an accelerated electron transport process. This phenomenon is brought about by the enhancement in the growth quality of InBr$_3$:CsPbBr$_3$ film and the reduction in the defects of Pb^{2+} and Br$^-$ after partial substitution of Pb^{2+} by In^{3+} or In cluster [25,39]. This is conducive to improving the V$_{OC}$ and fill factor (FF) of the devices [45].
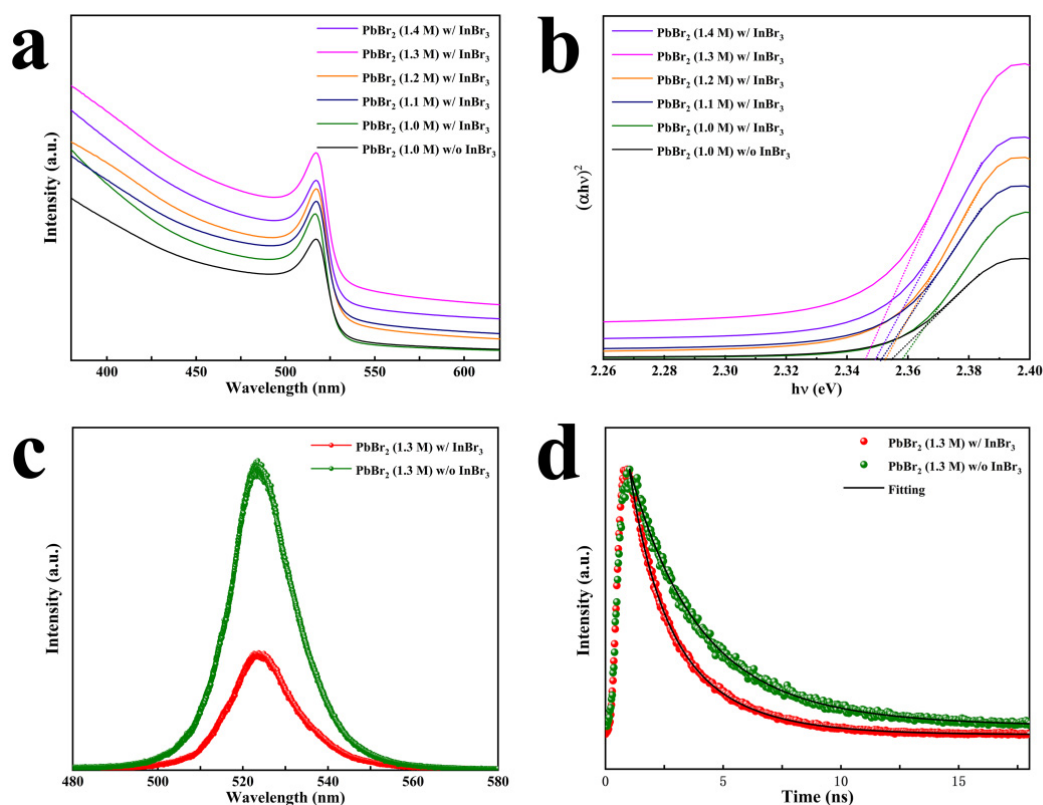

Figure 6. (**a**) UV–vis absorption spectra and (**b**) $(\alpha h \nu)^2$ vs. $h\nu$ plots for the InBr$_3$:CsPbBr$_3$ devices synthesized with different PbBr$_2$ concentrations; (**c**) PL and (**d**) TRPL decay spectra of InBr$_3$:CsPbBr$_3$ synthesized with the PbBr$_2$ concentration of 1.3 M.

4. Conclusions

By introducing InBr$_3$ into a PbBr$_2$ precursor solution, we successfully prepared planar carbon-based CsPbBr$_3$ solar cells with higher perovskite film quality in this work. The introduction of InBr$_3$ can transform the dense PbBr$_2$ film originally grown on c-TiO$_2$ into a porous structure. On this basis, appropriately increasing the PbBr$_2$ concentration in the DMF precursor solution can enhance the thickness of the CsPbBr$_3$ film and optimize the surface morphology without changing the phase of CsPbBr$_3$, which can effectively alleviate the low thickness and poor quality of the CsPbBr$_3$ film in the multi-step process.

Due to the increase in film thickness and the incorporation of In^{3+} or In cluster, the light absorption capacity of the $CsPbBr_3$ film is significantly improved. Therefore, the efficiency and EQE of the manufactured devices are significantly optimized. As $InBr_3$ is introduced into the current flooding fluid and the $PbBr_2$ concentration is 1.3 M, the small-area $CsPbBr_3$ solar cell has the best PCE, which is 5.76%, and the maximum EQE value is 83%. This work provides a certain reference for the preparation of high-quality $CsPbBr_3$ thin films, simplifying the structure and developing planar HTL-free $CsPbBr_3$ solar cells.

Supplementary Materials: The following are available online at https://www.mdpi.com/article/10.3390/nano11092408/s1, Figure S1: Cross-sectional SEM images of $PbBr_2$ films synthesized with different $PbBr_2$ concentration: (a) 1.0 M w/ $InBr_3$; (b) 1.1 M w/ $InBr_3$; (c) 1.2 M w/ $InBr_3$; (d) 1.3 M w/ $InBr_3$; (e) 1.4 M w/ $InBr_3$; Figure S2: Cross-sectional SEM images of $CsPbBr_3$ films synthesized with different $PbBr_2$ concentration: (a) 1.1 M w/o $InBr_3$; (b) 1.2 M w/o $InBr_3$; (c) 1.3 M w/o $InBr_3$; (d) 1.4 M w/o $InBr_3$; Figure S3: The schematic diagram of of 15 $CsPbBr_3$ PSCs synthesized with different $PbBr_2$ concentration: (a) JSC, (b) VOC, (c) FF and (e) PCE. Table S1: The average photovoltaic parameters of 15 $CsPbBr_3$ PSCs synthesized with different $PbBr_2$ concentration; Figure S4: PL spectra of the $InBr_3$:$CsPbBr_3$ synthesized with different $PbBr_2$ concentration; Table S2: The fitted data of TRPL characterization.

Author Contributions: K.C., X.M., and Q.L. conceived the idea; K.C. and X.M. performed research and analyzed data; K.C. drafted the manuscript; H.X., B.F., D.Y., and Q.L. provided assistance for data acquisition and data analysis. All authors have read and agreed to the published version of the manuscript.

Data Availability Statement: The data is available on reasonable request from the corresponding author.

Conflicts of Interest: The authors declare no conflict of interest.

References

1. Dunlap-Shohl, W.; Zhou, Y.; Padture, N.P.; Mitzi, D.B. Synthetic Approaches for Halide Perovskite Thin Films. *Chem. Rev.* **2019**, *119*, 3193–3295. [CrossRef]
2. Yuan, J.; Ling, X.; Yang, D.; Li, F.; Zhou, S.; Shi, J.; Qian, Y.; Hu, J.; Sun, Y.; Yang, Y.; et al. Band-Aligned Polymeric Hole Transport Materials for Extremely Low Energy Loss α-CsPbI3 Perovskite Nanocrystal Solar Cells. *Joule* **2018**, *2*, 2450–2463. [CrossRef]
3. Jeon, I.; Seo, S.; Sato, Y.; Delacou, C.; Anisimov, A.; Suenaga, K.; Kauppinen, E.I.; Maruyama, S.; Matsuo, Y. Perovskite Solar Cells Using Carbon Nanotubes Both as Cathode and as Anode. *J. Phys. Chem. C* **2017**, *121*, 25743–25749. [CrossRef]
4. Weber, S.; Rath, T.; Mangalam, J.; Kunert, B.; Coclite, A.M.; Bauch, M.; Dimopoulos, T.; Trimmel, G. Investigation of NiOX-hole Transport Layers in Triple Cation Perovskite Solar Cells. *J. Mater. Sci. Mater. Electron.* **2018**, *29*, 1847–1855. [CrossRef]
5. Chen, W.; Li, X.; Li, Y.; Li, Y. A review: Crystal Growth for High-Performance All-Inorganic Perovskite Solar Cells. *Energy Envi-ron. Sci.* **2020**, *13*, 1971–1996. [CrossRef]
6. Wang, K.; Liu, C.; Du, P.; Zhang, H.-L.; Gong, X. Efficient Perovskite Hybrid Solar Cells Through a Homogeneous High-Quality Organolead Iodide Layer. *Small* **2015**, *11*, 3369–3376. [CrossRef] [PubMed]
7. Yuan, S.; Qiu, Z.; Gao, C.; Zhang, H.; Jiang, Y.; Li, C.; Yu, J.; Cao, B. High-Quality Perovskite Films Grown with a Fast Solvent-Assisted Molecule Inserting Strategy for Highly Efficient and Stable Solar Cells. *ACS Appl. Mater. Interfaces* **2016**, *8*, 22238–22245. [CrossRef]
8. Hu, H.; Ren, Z.; Fong, P.W.; Qin, M.; Liu, D.; Lei, D.; Lu, X.; Li, G. Room-Temperature Meniscus Coating of >20% Perovskite Solar Cells: A Film Formation Mechanism Investigation. *Adv. Funct. Mater.* **2019**, *29*, 1900092. [CrossRef]
9. Liu, Z.; Deng, K.; Zhu, Y.; Wang, M.; Li, L. Iodine Induced PbI 2 Porous Morphology Manipulation for High-Performance Planar Perovskite Solar Cells. *Sol. RRL* **2018**, *2*, 1800230. [CrossRef]
10. Aristidou, N.; Eames, C.; Sanchez-Molina, I.; Bu, X.; Kosco, J.; Islam, M.S.; Haque, S.A. Fast oxygen diffusion and iodide defects mediate oxygen-induced degradation of perovskite solar cells. *Nat. Commun.* **2017**, *8*, 15218. [CrossRef]
11. Yen, H.-J.; Liang, P.-W.; Chueh, C.-C.; Yang, Z.; Jen, A.K.-Y.; Wang, H.-L. Large Grained Perovskite Solar Cells Derived from Single-Crystal Perovskite Powders with Enhanced Ambient Stability. *ACS Appl. Mater. Interfaces* **2016**, *8*, 14513–14520. [CrossRef] [PubMed]
12. Swarnkar, A.; Marshall, A.R.; Sanehira, E.M.; Chernomordik, B.D.; Moore, D.T.; Christians, J.A.; Chakrabarti, T.; Luther, J.M. Quantum dot-induced phase stabilization of -CsPbI3 perovskite for high-efficiency photovoltaics. *Science* **2016**, *354*, 92–95. [CrossRef] [PubMed]

13. Zhou, Y.; Game, O.S.; Pang, S.; Padture, N.P. Microstructures of Organometal Trihalide Perovskites for Solar Cells: Their Evolution from Solutions and Characterization. *J. Phys. Chem. Lett.* **2015**, *6*, 4827–4839. [CrossRef] [PubMed]

14. Ummadisingu, A.; Grätzel, M. Revealing the detailed path of sequential deposition for metal halide perovskite formation. *Sci. Adv.* **2018**, *4*, e1701402. [CrossRef]

15. Scherer, G.W. Stress from crystallization of salt. *Cem. Concr. Res.* **2004**, *34*, 1613–1624. [CrossRef]

16. Chen, Q.; Zhou, H.; Song, T.-B.; Luo, S.; Hong, Z.; Duan, H.-S.; Dou, L.; Liu, Y.; Yang, Y. Controllable Self-Induced Passivation of Hybrid Lead Iodide Perovskites toward High Performance Solar Cells. *Nano Lett.* **2014**, *14*, 4158–4163. [CrossRef]

17. Carmona, C.R.; Gratia, P.; Zimmermann, I.; Grancini, G.; Gao, P.; Graetzel, M.; Nazeeruddin, M.K. High efficiency methylammonium lead triiodide perovskite solar cells: The relevance of non-stoichiometric precursors. *Energy Environ. Sci.* **2015**, *8*, 3550–3556. [CrossRef]

18. Han, Q.; Ding, J.; Bai, Y.; Li, T.; Ma, J.-Y.; Chen, Y.-X.; Zhou, Y.; Liu, J.; Ge, Q.-Q.; Chen, J.; et al. Carrier Dynamics Engineering for High-Performance Electron-Transport-Layer-free Perovskite Photovoltaics. *Chem* **2018**, *4*, 2405–2417. [CrossRef]

19. Liu, T.; Hu, Q.; Wu, J.; Chen, K.; Zhao, L.; Liu, F.; Wang, C.; Lu, H.; Jia, S.; Russell, T.P.; et al. Mesoporous PbI2 Scaffold for High-Performance Planar Heterojunction Perovskite Solar Cells. *Adv. Energy Mater.* **2016**, *6*, 1501890. [CrossRef]

20. Dong, C.; Han, X.; Li, W.; Qiu, Q.; Wang, J. Anti-solvent assisted multi-step deposition for efficient and stable carbon-based CsPbI2Br all-inorganic perovskite solar cell. *Nano Energy* **2019**, *59*, 553–559. [CrossRef]

21. Zhao, Y.; Duan, J.; Wang, Y.; Yang, X.; Tang, Q. Precise stress control of inorganic perovskite films for carbon-based solar cells with an ultrahigh voltage of 1.622 V. *Nano Energy* **2020**, *67*, 104286. [CrossRef]

22. Tian, J.; Xue, Q.; Yao, Q.; Li, N.; Brabec, C.J.; Yip, H. Inorganic Halide Perovskite Solar Cells: Progress and Challenges. *Adv. Energy Mater.* **2020**, *10*, 2000183. [CrossRef]

23. Kulbak, M.; Gupta, S.; Kedem, N.; Levine, I.; Bendikov, T.; Hodes, G.; Cahen, D. Cesium Enhances Long-Term Stability of Lead Bromide Perovskite-Based Solar Cells. *J. Phys. Chem. Lett.* **2016**, *7*, 167–172. [CrossRef]

24. Zhang, J.; Hodes, G.; Jin, Z.; Liu, F. All-Inorganic CsPbX 3 Perovskite Solar Cells: Progress and Prospects. *Angew. Chem. Int. Ed.* **2019**, *58*, 15596–15618. [CrossRef] [PubMed]

25. Subhani, W.S.; Wang, K.; Du, M.; Wang, X.; Liu, F. Interface-Modification-Induced Gradient Energy Band for Highly Efficient CsPbIBr 2 Perovskite Solar Cells. *Adv. Energy Mater.* **2019**, *9*, 1803785. [CrossRef]

26. Duan, J.; Zhao, Y.; He, B.; Tang, Q. High-Purity Inorganic Perovskite Films for Solar Cells with 9.72% Efficiency. *Angew. Chem. Int. Ed.* **2018**, *57*, 3787–3791. [CrossRef]

27. Sun, K.; Hu, Z.; Shen, B.; Lu, C.; Huang, L.; Zhang, J.; Zhang, J.; Zhu, Y. Lewis Acid–Base Interaction-Induced Porous PbI2 Film for Efficient Planar Perovskite Solar Cells. *ACS Appl. Energy Mater.* **2018**, *1*, 2114–2122. [CrossRef]

28. Cao, J.; Wang, F.; Yu, H.; Zhou, Y.; Lu, H.; Zhao, N.; Wong, C.-P. Porous PbI2 films for the fabrication of efficient, stable perovskite solar cells via sequential deposition. *J. Mater. Chem. A* **2016**, *4*, 10223–10230. [CrossRef]

29. Jena, A.K.; Kulkarni, A.; Miyasaka, T. Halide Perovskite Photovoltaics: Background, Status, and Future Prospects. *Chem. Rev.* **2019**, *119*, 3036–3103. [CrossRef]

30. Meng, X.; Chi, K.; Li, Q.; Feng, B.; Wang, H.; Gao, T.; Zhou, P.; Yang, H.; Fu, W. Fabrication of Porous Lead Bromide Films by Introducing Indium Tribromide for Efficient Inorganic CsPbBr₃ Perovskite Solar Cells. *Nanomaterials* **2021**, *11*, 1253. [CrossRef]

31. Kato, Y.; Ono, L.K.; Lee, M.V.; Wang, S.; Raga, S.R.; Qi, Y. Silver Iodide Formation in Methyl Ammonium Lead Iodide Perovskite Solar Cells with Silver Top Electrodes. *Adv. Mater. Interfaces* **2015**, *7*, 1500195. [CrossRef]

32. Kulkarni, A.; Ünlü, F.; Pant, N.; Kaur, J.; Bohr, C.; Jena, A.K.; Öz, S.; Yanagida, M.; Shirai, Y.; Ikegami, M.; et al. Concerted Ion Migration and Diffusion-Induced Degradation in Lead-Free Ag₃BiI₆ Rudorffite Solar Cells under Ambient Conditions. *Sol. RRL* **2021**, *5*, 2100077. [CrossRef]

33. Domanski, K.; Correa-Baena, J.-P.; Mine, N.; Nazeeruddin, M.K.; Abate, A.; Saliba, M.; Tress, W.; Hagfeldt, A.; Grätzel, M. Not All That Glitters Is Gold: Metal-Migration-Induced Degradation in Perovskite Solar Cells. *ACS Nano* **2016**, *10*, 6306–6314. [CrossRef]

34. Schlipf, J.; Docampo, P.; Schaffer, C.J.; Körstgens, V.; Bießmann, L.; Hanusch, F.; Giesbrecht, N.; Bernstorff, S.; Bein, T.; Müller-Buschbaum, P. A Closer Look into Two-Step Perovskite Conversion with X-ray Scattering. *J. Phys. Chem. Lett.* **2015**, *6*, 1265–1269. [CrossRef]

35. Thompson, C.V. Solid-State Dewetting of Thin Films. *Annu. Rev. Mater. Res.* **2012**, *42*, 399–434. [CrossRef]

36. Yang, L.; Wang, J.; Leung, W.W.-F. Lead Iodide Thin Film Crystallization Control for High-Performance and Stable Solution-Processed Perovskite Solar Cells. *ACS Appl. Mater. Interfaces* **2015**, *7*, 14614–14619. [CrossRef] [PubMed]

37. Liu, X.; Tan, X.; Liu, Z.; Ye, H.; Sun, B.; Shi, T.; Tang, Z.; Liao, G. Boosting the efficiency of carbon-based planar CsPbBr₃ perovskite solar cells by a modified multistep spin-coating technique and interface engineering. *Nano Energy* **2019**, *56*, 184–195. [CrossRef]

38. Liu, C.; Li, W.; Li, H.-Y.; Wang, H.; Zhang, C.; Yang, Y.; Gao, X.; Xue, Q.; Yip, H.-L.; Fan, J.; et al. Structurally Reconstructed CsPbI2 Br Perovskite for Highly Stable and Square-Centimeter All-Inorganic Perovskite Solar Cells. *Adv. Energy Mater.* **2019**, *9*, 1803572. [CrossRef]

39. Wang, Z.-K.; Li, M.; Yang, Y.; Hu, Y.; Ma, H.; Gao, X.-Y.; Liao, L.-S. High Efficiency Pb-In Binary Metal Perovskite Solar Cells. *Adv. Mater.* **2016**, *28*, 6695–6703. [CrossRef] [PubMed]

40. Chen, L.; Wan, L.; Li, X.; Zhang, W.; Fu, S.; Wang, Y.; Li, S.; Wang, H.-Q.; Song, W.; Fang, J. Inverted All-Inorganic CsPbI2Br Perovskite Solar Cells with Promoted Efficiency and Stability by Nickel Incorporation. *Chem. Mater.* **2019**, *31*, 9032–9039. [CrossRef]

41. Ko, H.-S.; Lee, J.-W.; Park, N.-G. 15.76% efficiency perovskite solar cells prepared under high relative humidity: Importance of PbI2 morphology in two-step deposition of CH3NH3PbI3. *J. Mater. Chem. A* **2015**, *3*, 8808–8815. [CrossRef]
42. Chen, J.; Zhao, X.; Kim, S.; Park, N. Multifunctional Chemical Linker Imidazoleacetic Acid Hydrochloride for 21% Efficient and Stable Planar Perovskite Solar Cells. *Adv. Mater.* **2019**, *31*, 1902902. [CrossRef] [PubMed]
43. Yuan, H.; Zhao, Y.; Duan, J.; Wang, Y.; Yang, X.; Tang, Q. All-inorganic CsPbBr$_3$ perovskite solar cell with 10.26% efficiency by spectra engineering. *J. Mater. Chem. A* **2018**, *6*, 24324–24329. [CrossRef]
44. Pham, N.D.; Tiong, V.T.; Chen, P.; Wang, L.; Wilson, G.J.; Bell, J.; Wang, H. Enhanced perovskite electronic properties via a modified lead(ii) chloride Lewis acid–base adduct and their effect in high-efficiency perovskite solar cells. *J. Mater. Chem. A* **2017**, *5*, 5195–5203. [CrossRef]
45. Ma, J.; Yang, G.; Qin, M.; Zheng, X.; Lei, H.; Chen, C.; Chen, Z.; Guo, Y.; Han, H.; Zhao, X.; et al. MgO Nanoparticle Modified Anode for Highly Efficient SnO$_2$-Based Planar Perovskite Solar Cells. *Adv. Sci.* **2017**, *4*, 1700031. [CrossRef]